JGR Earth Surface

RESEARCH ARTICLE
10.1029/2019JF005419

Sediment Transit Time and Floodplain Storage Dynamics in Alluvial Rivers Revealed by Meteoric ^{10}Be

Marisa Repasch[1,2], Hella Wittmann[1], Joel S. Scheingross[1,3], Dirk Sachse[1], Ricardo Szupiany[4], Oscar Orfeo[5], Margret Fuchs[6], and Niels Hovius[1,2]

[1]German Research Centre for Geosciences GFZ, Potsdam, Germany, [2]Institute of Geosciences, University of Potsdam, Potsdam, Germany, [3]Department of Geological Sciences and Engineering, University of Nevada, Reno, Reno, NV, USA, [4]CONICET, College of Engineering and Water Sciences, Littoral National University, Santa Fe, Argentina, [5]CONICET, Center for Applied Ecology of the Littoral, Universidad Nacional de Nordeste, Corrientes, Argentina, [6]Helmholtz-Zentrum Dresden-Rossendorf, Helmholtz Institute Freiberg for ResourceTechnology, Freiberg, Germany

Key Points:
- Meteoric ^{10}Be measured in depth-integrated river suspended sediment geochemically records mean fluvial sediment transit time
- In the Rio Bermejo (Argentina), ^{10}Be concentrations increase 230% over ~1,300 km transit distance, yielding a mean total transit time of 8.4 ± 2.2 × 10^3 yr
- Reach-scale analysis of ^{10}Be-derived transit times shows that tectonics, channel migration rates, and incision depth are primary drivers

Supporting Information:
- Supporting Information S1

Correspondence to:
M. Repasch,
marisa.repasch@gfz-potsdam.de

Citation:
Repasch, M., Wittmann, H., Scheingross, J. S., Sachse, D., Szupiany, R., Orfeo, O., et al. (2020). Sediment transit time and floodplain storage dynamics in alluvial rivers revealed by meteoric ^{10}Be. *Journal of Geophysical Research: Earth Surface*, *125*, e2019JF005419. https://doi.org/10.1029/2019JF005419

Received 30 OCT 2019
Accepted 18 MAY 2020
Accepted article online 9 JUN 2020

Abstract Quantifying the time scales of sediment transport and storage through river systems is fundamental for understanding weathering processes, biogeochemical cycling, and improving watershed management, but measuring sediment transit time is challenging. Here we provide the first systematic test of measuring cosmogenic meteoric Beryllium-10 (^{10}Be$_m$) in the sediment load of a large alluvial river to quantify sediment transit times. We take advantage of a natural experiment in the Rio Bermejo, a lowland alluvial river traversing the east Andean foreland basin in northern Argentina. This river has no tributaries along its trunk channel for nearly 1,300 km downstream from the mountain front. We sampled suspended sediment depth profiles along the channel and measured the concentrations of ^{10}Be$_m$ in the chemically extracted grain coatings. We calculated depth-integrated ^{10}Be$_m$ concentrations using sediment flux data and found that ^{10}Be$_m$ concentrations increase 230% from upstream to downstream, indicating a mean total sediment transit time of 8.4 ± 2.2 kyr. Bulk sediment budget-based estimates of channel belt and fan storage times suggest that the ^{10}Be$_m$ tracer records mixing of old and young sediment reservoirs. On a reach scale, ^{10}Be$_m$ transit times are shorter where the channel is braided and superelevated above the floodplain, and longer where the channel is incised and meandering, suggesting that transit time is controlled by channel morphodynamics. This is the first systematic application of ^{10}Be$_m$ as a sediment transit time tracer and highlights the method's potential for inferring sediment routing and storage dynamics in large river systems.

Plain Language Summary Understanding how long sediment takes to travel downstream in rivers, also known as sediment "transit time," is crucial for responsible watershed management and constraining global biogeochemical cycles. We aim to measure transit times for large rivers and determine the processes regulating this time scale. We present a new transit time proxy based on beryllium-10 (^{10}Be), a rare isotope produced in the atmosphere and delivered to Earth by rain. If river sediment collected downstream has more ^{10}Be than sediment upstream, this indicates that sediment was trapped in the floodplain for many years before continuing to travel downstream. We collected river sediment at multiple locations from upstream to downstream along a large, undammed river, the Rio Bermejo in Argentina. We found that ^{10}Be increased 230% from upstream to downstream, translating to a transit time of ~8,500 years. This long time scale implies that sediment and carbon delivered to rivers have enough time to be weathered or oxidized to CO_2 before they are buried in the ocean. We also show that transit time is controlled by the river's shape and lateral mobility, suggesting that human alteration of channel shape or sediment supply will reduce a river's ability to use its floodplain for natural flood and erosion control.

1. Introduction

The residence time of sediment at Earth's surface influences multiple time-dependent processes, including soil formation, weathering, nutrient production, and biogeochemical cycling. Furthermore, sediment deposition and remobilization during source-to-sink transit can dampen or transform sedimentary signals produced by discrete episodic events (Armitage et al., 2011; Jerolmack & Paola, 2010; Pizzuto et al., 2017), conflating the record of climatic and tectonic forcing preserved in sedimentary archives. Knowing the

amount of time river sediment takes to travel from source to sink is essential to understand the effects that can accumulate during transit and to elucidate the processes that regulate routing pathways.

In this study, we explore fluvial sediment "transit time," which we define as the mean time required for all sedimentary particles delivered to a river channel to be conveyed downstream to the river's outlet, including time spent in transient storage in the channel margins. Our main objectives are to (1) quantify transit times using a geochemical proxy, and (2) determine the geomorphic and/or tectonic mechanisms regulating sediment transit time.

Various proxy methods have been tested to resolve sediment transit time in river systems, which have progressively improved our ability to quantify the rate of sediment transit. Uranium series isotopes provide a chronometer for the time since sediment reached 63 μm or smaller and have been used to estimate river sediment transit times and comminution ages (e.g., Depaolo et al., 2006; Dosseto et al., 2008; Granet et al., 2010). However, this method cannot estimate transit time for larger grain size fractions that are common in many rivers, and newer studies identify that small changes to input parameters of U-series comminution age models, such as the uranium leaching rate, result in large uncertainties in transit time estimates (e.g., Handley et al., 2013; Martin et al., 2019). Luminescence has also been explored as a tracer of fluvial sediment transport (Gray et al., 2017, 2018), based on the idea that sediment is bleached (re-set) during transport and regenerated during storage. However, tests of this model yielded long-term storage times and transport length scales inconsistent with values derived from sediment budget-based methods (Gray et al., 2017). These previous efforts highlight the need for additional transit time proxies that are sensitive on time scales of 10^3–10^5 yr and can yield results commensurate with geomorphic data.

Fluvial sediment transit times have also been approximated using theoretical models (e.g., Bradley & Tucker, 2013; Lauer & Parker, 2008; Pizzuto et al., 2014), but thus far these theories are developed for steady-state, mass-balanced rivers. Transit time can be influenced by a number of processes, including channel length and steepness, its morphology and dynamics (e.g., vertical incision, lateral migration), the balance of sediment supply to transport capacity, accommodation space, and the frequency of channel breaching and avulsion (Dade & Friend, 1998; Lauer & Parker, 2008; Phillips et al., 2007; Sheets et al., 2002; Strong et al., 2005). As a result, simple, steady-state modeling approaches to estimate sediment transit time are often not representative of a system's dynamic response to periodic climatic or tectonic change. For example, in actively developing foreland basins, dynamic processes including foredeep subsidence, forebulge uplift, and backbulge subsidence drive rivers to aggrade, incise, and distribute sediment differentially across the lowland (Lane & Richards, 1997). How such tectonic and geomorphic processes influence sediment transit time is largely unknown, due to the lack of suitable techniques to track sediment over ~10^3–10^5 yr time scales during which these processes play out. Once transit times can be estimated with higher precision, we can study how morphodynamic processes influence the duration of sediment transport and storage.

In this study we systematically test the use of meteoric ^{10}Be ($^{10}Be_m$) in river sediment as a proxy for fluvial sediment transit time. We measure $[^{10}Be]_m$ in river sediment sampled from river depth profiles along the Rio Bermejo, a large alluvial river traversing the East Andean foreland in northern Argentina. We use these data to calculate the change in $[^{10}Be]_m$ with distance downstream from the mountain front and thereby estimate the transit time for sediment moving across the lowland basin. To support that the $^{10}Be_m$ proxy provides reasonable transit time estimates, we compare our $^{10}Be_m$-derived transit time to theoretical short and long time scale transit times estimated with sediment budgeting methods. We evaluate the controls on sediment transit time by comparing four reaches of the mainstem Rio Bermejo, which have distinct differences in channel planform, incision depth, and lateral migration rate, and sit in different morphotectonic domains of the Andean foreland basin.

2. Meteoric ^{10}Be as a Transit Time Proxy

$^{10}Be_m$ has potential to trace sediment transit over large spatial and temporal scales. $^{10}Be_m$ is a cosmogenic radionuclide produced in Earth's atmosphere through the bombardment of nitrogen and oxygen atoms by cosmic rays (Lal & Peters, 1967), with a half-life of 1.387×10^6 yr (Chmeleff et al., 2010; Korschinek et al., 2010), which is sufficiently long such that radioactive decay is negligible over 10^4 yr or less. After production in the atmosphere, $^{10}Be_m$ is captured by water vapor and aerosol particles and then delivered to

Earth's surface primarily through precipitation and aerosol deposition (Willenbring & von Blanckenburg, 2010). As a cation, $^{10}Be_m$ is adsorbed onto mineral surfaces and is incorporated into the secondary mineral coatings on all sedimentary particles, particularly oxyhydroxides. To measure $^{10}Be_m$ concentrations, these coatings, or "reactive phases," can be easily detected in as little as 0.5 g of sediment with heterogeneous mineralogy.

$^{10}Be_m$ concentrations have been measured to determine soil residence time, and rates of erosion, weathering, and denudation (e.g., Egli et al., 2010; Jelinski et al., 2019; von Blanckenburg et al., 2012; Wittmann et al., 2015). Monaghan et al. (1983) first explored $^{10}Be_m$ as a soil residence time chronometer, demonstrating that the inventory of $^{10}Be_m$ derived from its accumulation in soil profiles correlates with soil age, and is retained within soil profiles over 10^4–10^6 yr time scales. When soil profile age is known, the inventory of $^{10}Be_m$ in the soil profile can be used to derive a local $^{10}Be_m$ depositional flux ($F^{10}Be_m$) (e.g., Graly et al., 2011).

We employ a similar concept here, but use the inventory of $^{10}Be_m$ in river sediment load to estimate the average time sediment particles are stored within the river system before being exported, which we term "transit time." Sediment stored in the river banks and floodplain receives a local $F^{10}Be_m$ (at m^{-2}) at the surface, and over time, this $^{10}Be_m$ is redistributed down the sediment profile. In a laterally-migrating river system, sediment is frequently deposited on the floodplain and remains there for many years before being reentrained. Particles remobilized from storage have $^{10}Be_m$ concentrations ($[^{10}Be]_m$) representing the cumulative storage time. The depth to which the channel remobilizes stored sediment is defined as the "remobilization depth," h, which ultimately determines how much active channel sediment is exchanged with floodplain sediment. Increasing h, along with channel migration rate, increases the probability that sediment is stored during transit. Accordingly, the net sediment transit time increases with progressively more lateral sediment exchange along the channel. This net transit time is recorded by $[^{10}Be]_m$ in active channel sediment, which should increase downstream at a corresponding rate. We assume the addition of $^{10}Be_m$ during active in-channel transport is negligible because time spent in motion is a small fraction of the total transit time (Pizzuto et al., 2014).

The validity of this concept has been shown by Wittmann et al. (2015), who showed that measured $^{10}Be_m$ concentrations in depth-integrated river sediment profiles in the Amazon River basin increase substantially through ~1,000 km of downstream transit. This increase validates the concept of using $^{10}Be_m$ to measure transit time, but interpreting the data in terms of a sediment transit time yields a large range of uncertainty (1.6 to 29 kyr), largely due to insufficient quantification of the remobilization depth. To reduce uncertainty and to realize the potential of this approach, the transit time estimate requires additional geomorphic data, such as the depth of incision, channel migration rates, and increased spatial resolution of $^{10}Be_m$ measurements.

River sediment $^{10}Be_m$ concentration data may be a powerful tool for catchment scale sediment dynamics studies (e.g., Belmont et al., 2014; Rahaman et al., 2017; Reusser & Bierman, 2010; Stout et al., 2014; Wittmann et al., 2015). However, $[^{10}Be]_m$ in sediment is dependent on specific surface area (SSA) and the composition and abundance of grain coatings (Shen et al., 2004; Singleton et al., 2017). SSA relates inversely to grain size, and thus is subject to hydrodynamic particle sorting in rivers (Rouse, 1937). This can be accounted for by calculating depth-integrated concentrations based on samples collected from full river water depth profiles (Bouchez et al., 2011; Wittmann et al., 2015, 2018). Many lowland rivers also experience downstream particle size fining (e.g., Frings, 2008; Sternberg, 1875) and weathering, which may increase downstream $^{10}Be_m$ sorption capacity and abundance of grain coatings, respectively, causing apparently longer transit times. To correct for downstream changes in SSA and secondary mineral abundance, $[^{10}Be]_m$ can be normalized to concentrations of reactive phase Beryllium-9 ($^9Be_{reac}$). $^9Be_{reac}$ exhibits similar geochemical behavior as $^{10}Be_m$, but its supply is limited by weathering and reactive transport, whereas $^{10}Be_m$ is continuously supplied via atmospheric delivery (von Blanckenburg et al., 2012). If both SSA and $[^{10}Be]_m$ increase downstream, but $[^9Be]_{reac}$ does not, then these effects have no control on Be concentrations, and increases in $[^{10}Be]_m$ are exclusively due to increasing transit time.

3. Study Area and Sampling

3.1. Rio Bermejo, Andean Foreland Basin

An ideal setting to study source to sink transit time is a river system with a single, well-constrained sediment source, and one long, channel without tributaries or distributaries that interacts with its floodplain by

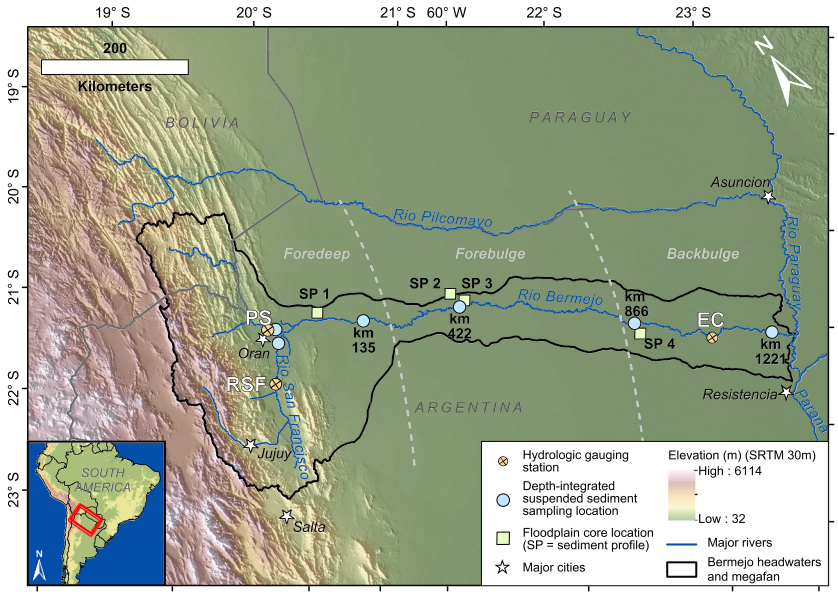

Figure 1. Overview shaded relief map of the Rio Bermejo fluvial system in the Andean foreland basin of NW Argentina. Inset map shows the location in the South American continent. The thick black line delineates the extent of the Rio Bermejo headwaters and the extent of the megafan in the lowland basin, which is not equivalent to the flow-routed drainage area. Dark blue lines show only the rivers relevant to this study. Pale blue circles show the locations of the six suspended sediment depth profiles, labeled with their distance downstream along the channel in kilometers. Pale green squares mark the locations of sediment profile (SP) samples. Pale orange quartered circles represent three hydrologic gauging stations: PS = Pozo Sarmiento, RSF = Rio San Francisco, EC = El Colorado. Gray dashed lines show the approximated boundaries between the foredeep, forebulge, and backbulge depozones.

overbank flow and lateral migration. The Rio Bermejo in northern Argentina (Figure 1) is a unique setting where a high sediment flux delivered from the Andes is conveyed through a lowland basin along a ~1,300 km channel with no tributaries. At the mountain front, headwater streams draining the eastern Andes fold-and-thrust belt converge into one trunk channel—the mainstem Rio Bermejo. The Rio San Francisco (RSF) is the last major tributary to deliver water and sediment to the Bermejo near the mountain front (river km 0), after which the river runs 1,267 river km downstream (nearly 700 km linear distance from the mountain front) before reaching the Rio Paraguay. Sediment sourced upstream of the RSF confluence can only be transported downstream or deposited in the channel margins and is not mixed with tributary inputs, making the Rio Bermejo an ideal natural laboratory to study long distance sediment transit.

Repeated avulsions of the Rio Bermejo since the late Pleistocene have given rise to a narrow fluvial megafan extending from the Andean mountain front to the valley of the Rio Paraguay (Iriondo, 2007). Despite subtle, low-relief topography, the modern channel belt is perched atop this megafan, preventing tributaries from joining the river. The headwaters and megafan comprise an area of 120,280 km^2, of which 70,000 km^2 belongs to the megafan (Figure 1).

Previous studies identify three distinct depozones across the megafan (Figure 1), related to lithospheric flexure in the periphery of the Andean orogen (Cohen et al., 2015; Horton & DeCelles, 1997; Horton & Decelles, 2001; McGlue et al., 2016), which appear to influence the morphodynamics, and potentially the sediment transit time, of the Rio Bermejo. After exiting the mountain front, the river traverses the foredeep basin for ~175 km, where the channel is braided and ~1.5 m deep. In this reach, persistent aggradation has lifted the active channel belt above the surrounding lowland. Downstream from the foredeep, the river encounters a zone of forebulge uplift, where the channel abruptly transitions to a single-thread meandering planform with a channel depth of ~5 m, a cut bank height of up to 8 m, and high channel migration rates of 10–50 m yr^{-1}, as estimated from time-series satellite image analysis (Text S1). This pattern persists from ~175 to ~450 km east of the mountain front, where the river enters the backbulge depozone. There the channel is variably superelevated and incised as it traverses previous channel belts, the average channel migration rate

is <10 m yr^{-1}, and lateral erosion is restricted to separate short reaches along the river (Text S1). We use $^{10}Be_m$ to evaluate the differences in transient storage time within and across these three depozones.

A first-order control on the amount of $^{10}Be_m$ in the river sediment load is the modern erosional flux from upstream. Water and suspended sediment discharge records are available at three gauging stations in the lower Rio Bermejo system (PS, RSF, and EC on Figure 1), which allow us to evaluate water and sediment fluxes from upstream to downstream (see Text S1). Analysis of gauging station data suggest that 86% of the suspended sediment delivered to the mainstem Rio Bermejo is eroded from the northern half of the headwaters, and only 14% of the sediment flux is derived from the RSF catchment, despite roughly equal drainage areas. Total annual sediment flux calculated for the Rio Bermejo just downstream of the RSF confluence is 103 Mt yr^{-1}, while 80 Mt yr^{-1} is recorded at EC (Text S1). This upstream-downstream disparity reflects the loss of 23% of sediment load to storage in the foredeep basin, while 80 Mt yr^{-1} of sediment transits the megafan.

3.2. River Sediment and Floodplain Profile Sampling

To estimate the mean transit time of sediment conveyed by the Rio Bermejo, we measured [$^{10}Be_m$] in suspended sediment collected at multiple locations along the mainstem and evaluated the change in concentration from upstream to downstream. We then determined the time required to accumulate the additional $^{10}Be_m$, given the local $F^{10}Be_m$. We constrained this local depositional flux by using independently dated (OSL) floodplain soil profiles (see below).

We collected fluvial suspended sediment in vertical depth profiles at five sampling locations along the length of the Rio Bermejo (Figure 1) during near-bankfull conditions, when discharge varied between 675 and 1,080 $m^3\ s^{-1}$ and banks were actively eroding. Additionally, we collected one depth profile from RSF and one from the Rio Bermejo 10 km upstream of the RSF confluence. We calculated an integrated headwater depth profile by combining these profiles upstream of the mainstem and weighting them by their respective proportions of the total sediment load input to the mainstem. We located the channel thalweg at each sampling location using a 600 kHz ADCP (Acoustic Doppler Current Profiler, Teledyne Workhorse). In the thalweg, we collected water and suspended sediment from a boat using a weighted 8-L horizontal sampling bottle (Wildco Beta Plus bottle) with an attached pressure transducer to measure sampling depth. To capture the range and distribution of grain sizes and sediment concentrations in the river, suspended sediment samples were collected from two to four discrete depths within a vertical profile and complemented with a bed sediment sample collected using a weighted sampling net, when possible.

Sediment-laden water was transferred from the sampling bottle to 15 liter vessels for interim storage prior to filtration. We separated sediment from the water using a custom-built 5-L pressurized filtration unit with a 293 mm diameter, 0.2 μm polyethersulfone filter. Sediment remained on the filters and was stored in combusted amber glass bottles for shipping. Bed sediment samples were stored in sterile plastic bags. In the laboratory, we rinsed sediment off the filters directly into an evaporating dish with ultrapure 18.2 MΩ water (pH ~ 7; when needed, we added NH_3 solution to the water to maintain pH ~ 7). Samples were dried in an oven at 40°C, and subsequently homogenized.

To determine the local $F^{10}Be_m$, we measured [$^{10}Be_m$] in sediment samples collected from four OSL-dated floodplain sediment depth profiles along the megafan (Figure 1). To simplify the OSL age determination, we attempted to sample paleochannel point bars, under the assumption that these areas have experienced rapid sediment deposition such that the time scale of deposit formation may be less than the error associated with OSL measurements. We used a stainless-steel hand auger to collect sediment down to a maximum depth of ~5 m. For $^{10}Be_m$ and $^{9}Be_{reac}$ analysis, we extracted samples that integrated material from 0–20 cm below the surface, 20–50 cm, and regularly spaced 40 cm intervals for lower depths. We homogenized the material prior to packing into clean plastic bags. For OSL analysis, we collected light-sealed samples by driving an opaque tube into our floodplain cores at select depths (see Text S3 for complete OSL methods).

4. Methods

4.1. Grain Size and Specific Surface Area Analysis

Sediment particle size distributions were measured on ~10 mg aliquots using a laser diffraction particle size analyzer (Horiba LA-950). Ten replicate measurements were made for each sample. Using the mean of the

10 measured grain size distributions, we calculated the 50th percentile value (D_{50}) and the fraction of silt and clay as the fraction of sample with grain size diameter <63 μm.

Specific surface area (SSA) of bulk sediment samples was measured on ~4 g aliquots using a Quantachrome NOVAtouch LX gas sorption analyzer. For each sample, a linear adsorption isotherm was calculated using measurements at five pressure conditions, and SSA was determined using the Brunauer, Emmett, and Teller (BET) theory (Brunauer et al., 1938). R^2 values for all BET isotherms used to calculate SSA were greater than 0.9997.

4.2. Extraction and Measurement of $^{10}Be_m$ and $^{9}Be_{reac}$

Sediment aliquots (0.5–1 g) were oven-dried overnight at 110°C, and immediately weighed. The total reactive phase, including amorphous oxyhydroxides and crystalline oxide grain coatings, was extracted from the sediment samples using a procedure adapted from Wittmann et al. (2012). ^{10}Be was purified from the extracted material, spiked with a ^{9}Be carrier solution containing 150 μg of ^{9}Be, and packed into targets for AMS measurement at the University of Cologne Centre for Accelerator Mass Spectrometry (Cologne, Germany). ^{10}Be/^{9}Be measurements were normalized to the KN01-6-2 and KN01-5-3 standards (Dewald et al., 2013) that are consistent with a ^{10}Be half-life of 1.36 ± 0.07 × 10^6 yr^{-1} (Nishiizumi et al., 2007). $[^{10}Be]_m$ was calculated from the normalized and blank-corrected ^{10}Be/^{9}Be ratios. The reported 1σ uncertainties include counting statistics and the uncertainties of both standard normalization and blank correction. Stable ^{9}Be concentrations were measured on a separate aliquot of the sample solution using inductively coupled plasma optical emission spectroscopy (ICP-OES). Uncertainty of ICP-OES measurements was 5%.

4.3. River Profile Depth-Integration

To account for variability in $[^{10}Be]_m$ with sampling depth due to hydrodynamic sorting, we calculated depth-integrated $[^{10}Be]_m$ ($[^{10}Be]_{m\text{-}DI}$) for each river depth profile following the approach of Wittmann et al. (2018). We modified the method by using the relationship between $[^{10}Be]_m$ and specific surface area, rather than grain size. For each river depth profile, we estimated the depth-integrated suspended sediment concentration (SSC_{DI}) used a Rouse-type model (Rouse, 1937), following the approach presented in Bouchez et al. (2011). After determining SSC_{DI} for each profile, we calculated depth-integrated SSA (SSA_{DI}) using linear regressions between individual SSC and SSA measurements in each depth profile, following

$$SSA_{DI} = m * SSC_{DI} + b, \quad (1)$$

where m and b are the slope and y intercept, respectively, of the linear regression for SSC and SSA modeled for each depth profile. Depth-integrated nuclide concentrations were calculated for each depth profile by solving for $[^{10}Be]_m$ and $[^{9}Be]_{reac}$ as a function of the SSA, following

$$[N]_{DI} = n * SSA_{DI} + c, \quad (2)$$

where $[N]_{DI}$ represents the depth-integrated concentration of a given nuclide, and n and c are the slope and y-intercept, respectively, of the linear regression for SSA and $[N]$ calculated for each depth profile. Uncertainty is quantified using the root mean square error of the linear regression for $[N]$ and SSA. Because we could not collect samples directly downstream of the RSF confluence, we calculated headwater-integrated $[^{10}Be]_m$ and $[^{9}Be]_{reac}$ values for the mainstem Rio Bermejo at river km 0. We weighted both $[^{10}Be]_{m\text{-}DI}$ and $[^{9}Be]_{reac\text{-}DI}$ by the modern sediment discharges of the two tributary channels.

We then use the $(^{10}Be/^{9}Be)_{reac}$ ratio to correct for SSA and secondary metal effects on $[^{10}Be]_m$ in river sediment (von Blanckenburg et al., 2012; Wittmann et al., 2012). Following this approach, we effectively isolate the depth-integrated $^{10}Be_m$ signal along the river transect by normalizing $[^{10}Be]_m$ values to the river-averaged $[^{9}Be]_{reac}$, which is relatively uniform along the river transect (Figure 2) using

$$\left[{}^{10}Be\right]_{\mathrm{norm}x=n} = \left(\frac{\left[{}^{10}Be\right]}{\left[{}^{9}Be\right]}\right)_{\mathrm{reac},x=n} * \overline{\left[{}^{9}Be\right]_{\mathrm{reac-riv}}}. \quad (3)$$

Here, $[^{10}\mathrm{Be}]_{\mathrm{norm}}$ is the normalized $^{10}\mathrm{Be_m}$ concentration (now independent of SSA), $(^{10}\mathrm{Be}/^{9}\mathrm{Be})_{\mathrm{reac}}$ is the ratio for a given sampling location x, and $\overline{[^{9}Be]}_{\mathrm{reac\text{-}riv}}$ is the average of all $[^{9}\mathrm{Be}]_{\mathrm{reac}}$ values measured in river sediment. The resulting $[^{10}\mathrm{Be}]_{\mathrm{norm}}$ value is then used to estimate average transit times for the bulk sediment load.

4.4. Estimation of Local $F^{10}Be_m$ From Floodplain Sediment Profiles

The globally-averaged $F^{10}\mathrm{Be_m}$ is ~1.09×10^6 atoms $\mathrm{cm^{-2}\ yr^{-1}}$ derived from time-averaged general circulation model (GCM) runs (Heikkila & von Blanckenburg, 2015). These authors combined modern ("industrial" conditions) and early Holocene ("pre-industrial" conditions) models for ^{10}Be deposition to produce time-averaged estimates of $F^{10}\mathrm{Be_m}$. These two models have large differences that may result from strong precipitation gradients at the eastern flank of the Andes, or time-variable moisture circulation patterns. Therefore we estimated a representative $F^{10}\mathrm{Be_m}$ for the Rio Bermejo floodplain, using measured $^{10}\mathrm{Be_m}$ inventories in dated soil profiles (Reusser et al., 2010). $F^{10}\mathrm{Be_m}$ (at $\mathrm{cm^{-2}\ yr^{-1}}$) was calculated following a method adapted from Willenbring and von Blanckenburg (2010):

$$F^{10}Be_m = \frac{\left[\int_{z=0}^{z}\left(\left[{}^{10}Be\right]_{m,z} - \left[{}^{10}Be\right]_{m,i}\right)\rho_s\, dz\right]\lambda}{\left(1 - e^{-\lambda t}\right)}. \quad (4)$$

The numerator gives the sediment or soil inventory of reactive ^{10}Be (at $\mathrm{cm^{-2}}$), z is the depth below the surface (cm), ρ_s is the sediment bulk density ($\mathrm{g\ cm^{-3}}$), $[^{10}\mathrm{Be}]_{\mathrm{m,z}}$ is the measured concentration (at $\mathrm{g^{-1}}$) for a sampled depth interval, and $[^{10}\mathrm{Be}]_{\mathrm{m,i}}$ is the ^{10}Be concentration (at $\mathrm{g^{-1}}$) inherited from previous floodplain storage events experienced by the sediment prior to deposition at the sample location. We estimate the value of this inherited $^{10}\mathrm{Be_m}$ as the ^{10}Be concentration measured in modern active channel sediment sampled just upstream of the sediment profile location, $[^{10}\mathrm{Be}]_{\mathrm{m,i}}$ (at $\mathrm{g^{-1}}$), assuming this inherited concentration has been constant through time. To derive $F^{10}\mathrm{Be_m}$, we divide the inventory by t, the sediment depositional age (yr), while accounting for radioactive decay with the ^{10}Be decay constant, λ.

4.5. Estimation of Fluvial Sediment Transit Time From $[^{10}\mathrm{Be}]_m$

Using $^{10}\mathrm{Be_m}$ as a proxy for fluvial sediment transit time was suggested by Wittmann et al. (2015), who tested this approach on the Amazon River system. Their model is based on the soil $^{10}\mathrm{Be_m}$ inventory equation of Willenbring and von Blanckenburg (2010). In principle, river suspended sediment at the mountain front begins its journey downstream with an inherited $[^{10}\mathrm{Be_m}]$, and any additional $^{10}\mathrm{Be_m}$ adsorbed to the sediment records time particles spend in storage as they travel downstream. $^{10}\mathrm{Be_m}$ accumulates in river sediment at a rate proportional to its transit time, under the assumption that (1) the local $F^{10}\mathrm{Be_m}$ is spatially constant along the river and is constant through time, (2) particles stored in the floodplain incorporate $^{10}\mathrm{Be_m}$ into their secondary mineral coatings at a rate consistent with $F^{10}\mathrm{Be_m}$, and (3) the channel exchanges sediment with stored floodplain sediment at a uniform rate through time via lateral channel migration and avulsions. Under these conditions, a net downstream increase in $[^{10}\mathrm{Be_m}]$ represents added floodplain storage time, which can be solved for.

Here we estimate the sediment transit time through the Rio Bermejo from the mountain front to river km 1,221 using depth-integrated $^{10}\mathrm{Be_m}$ measurements for the total suspended load. Following Wittmann et al. (2015), we model the evolution of $^{10}\mathrm{Be_m}$ in river sediment through time, using:

$$I_{^{10}Be_m}(t) = F\frac{^{10}Be_m}{\lambda}\left(1 - e^{-\lambda t}\right) + \left[{}^{10}Be_m\right]_{x=0} * \rho_s * h * e^{-\lambda t}, \quad (5)$$

where $I_{^{10}Be_m}$ is the measured $^{10}\mathrm{Be_m}$ inventory (at $\mathrm{m^{-2}}$) at a downstream sampling site, given by Equation 6:

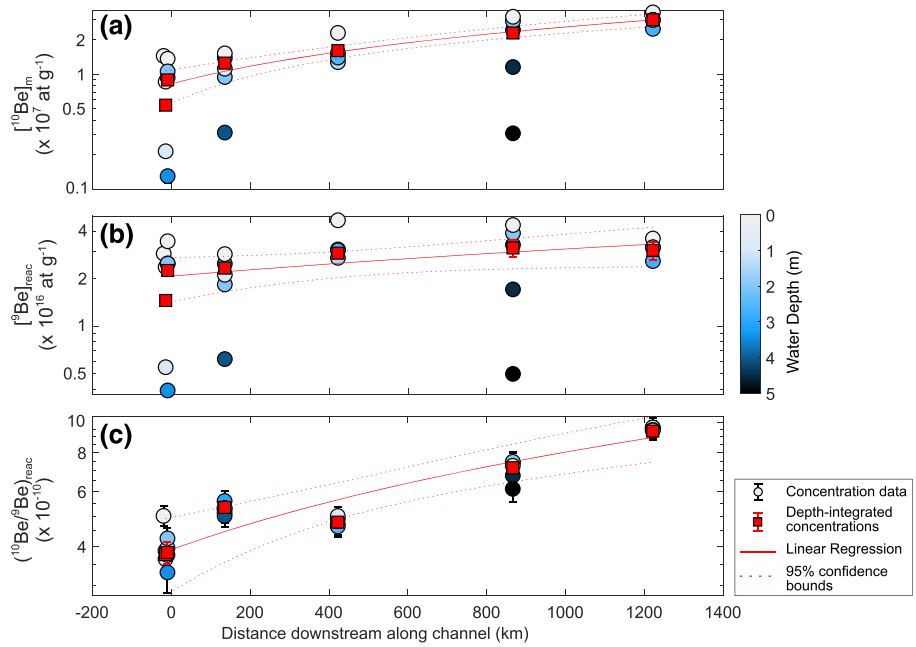

Figure 2. Downstream trends in (a) $[^{10}Be]_m$, (b) stable $[^{9}Be]_{reac}$, and (c) $(^{10}Be/^{9}Be)_{reac}$. Circles represent individual samples, colored by depth below the water surface at the sampling location (total water depth differs among locations). Red squares show the depth-integrated values. The red trend lines show the linear regressions with 95% confidence intervals calculated for the depth-integrated samples. Error bars for individual samples represent the analytical uncertainty, and error bars on the depth-integrated values represent the root-mean-square errors for the depth-integration models.

$$I_{^{10}Be_{m_{x=n}}} = \left[^{10}Be_m\right]_{x=n} * \rho_s * h. \quad (6)$$

In Equations 5 and 6, t is the mean time (yr) passed since the sampled sediment entered the river at distance $x = 0$, h is the remobilization depth (m) to which the river laterally erodes into floodplain sediment, and ρ_s is the bulk sediment density (kg m^{-3}). F$^{10}Be_m$ is the flux of $^{10}Be_m$ from the atmosphere to the floodplain, derived from Equation 4 and sediment profile concentration data. The two terms on the right side of Equation 5 represent first, the supply and decay of $^{10}Be_m$ to stored floodplain sediment via atmospheric deposition, and second, the radioactive decay of $^{10}Be_m$ in sediment supplied from upstream and collected at the sampling point. This equation assumes that all variables are invariant through time. $I_{^{10}Be_m}$ will be smaller if particles comprising the sample passed downstream without storage, and thus the mean particle transit time derived from Equation 5 will be shorter. The opposite is true for particles stored during transit.

5. Results

5.1. Grain Size Distributions and Specific Surface Area

The depth-integrated D_{50} of suspended sediment ranged from 142 μm in the depth profile sampled upstream of the RSF confluence to 9 μm at river km 1,221 (Table S1). The D_{50} of river bed sediment ranged from 325 μm at river km 0 to 160 μm at river km 866. The fraction of silt and clay in the river load (f_{s+c}) showed patterns similar to the grain size. Depth-integrated f_{s+c} was 0.33 at the confluence and increased to 0.92 at km 1,221 (Table S1).

SSA values follow an inverse power law relationship with grain size (Figure S1, Text S2). SSA ranged from 1.16 m^2 g^{-1} for the coarsest sample (D_{50} 325 μm) to 22.49 m^2 g^{-1} for the finest sample (D_{50} 7.8 μm). Depth-integrated SSA increased by nearly a factor of three from upstream to downstream (7 to 21 m^2 g^{-1}, Table S1). SSA of river bed sediment did not change strongly from upstream to downstream (Table S1). SSA normalized by D_{50} (SSA/D_{50}) for individual samples exhibited strong gradients within river depth

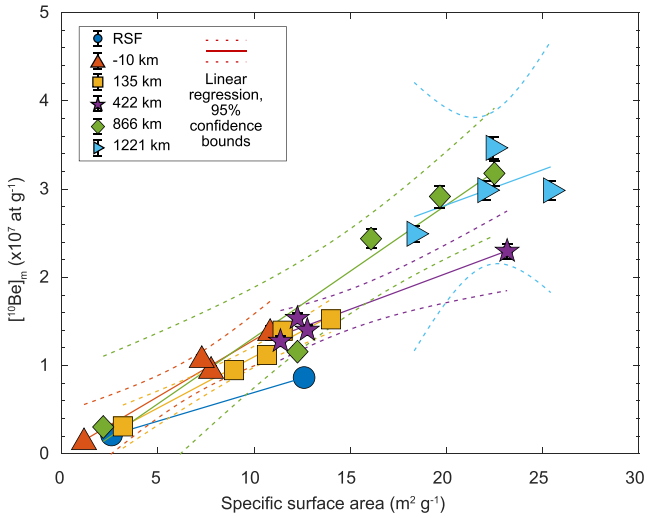

Figure 3. Relationship between $[^{10}Be]_m$ (atoms g^{-1} dry sediment) and specific surface area (m^2 g^{-1} dry sediment) for each suspended sediment sample. Colors and symbols differentiate the depth profiles at multiple locations along the Rio Bermejo. Trend lines represent linear regressions and 95% confidence intervals for each depth profile. The coefficients of these regressions were used to calculate the depth-integrated $[^{10}Be]_{m\text{-}DI}$ values.

profiles, indicating a range of particle shapes. Surface suspended sediment samples had the highest SSA/D_{50} ratio, and bed sediment exhibited the lowest ratios (Figure S3).

5.2. Beryllium Isotopes in River Sediment Depth Profiles

$[^{10}Be]_m$ was lowest at the upstream sampling locations, where the RSF values ranged from 0.21×10^7 to 0.86×10^7 at g^{-1} and the Bermejo upstream of the confluence ranged from 0.13×10^7 to 1.37×10^7 at g^{-1} (Table S2). $[^{10}Be]_m$ increased with distance downstream of the confluence, and the highest concentrations were observed at river km 1,221, where values ranged from 2.49×10^7 to 3.47×10^7 at g^{-1} (Figure 2a, Table S2). $[^{9}Be]_{reac}$ ranged from 0.39×10^{16} at g^{-1} to 4.7×10^{16}, but did not exhibit clear trends from upstream to downstream (Figure 2b, Table S2). $(^{10}Be/^{9}Be)_{reac}$, exhibited significantly reduced variability among samples at a single site compared to individual $[^{10}Be]_m$ values and shows a clear increase with distance downstream (Figure 2c, Table S2).

Hydrodynamic sorting of river suspended sediment created strong gradients in both $[^{10}Be]_m$ and $[^{9}Be]_{reac}$ with depth in the water column (Figures 2a and 2b), due to particle surface area dependence. $[^{10}Be]_m$ exhibited a strong linear relationship with SSA (mean $R^2 = 0.9390$) (Figure 3), with the lowest concentrations in river bed sediment and the highest concentrations in surface water suspended sediment. Depth-integrated values were calculated by weighting $[^{10}Be]_m$ by sediment concentrations in the river water (SSC), according to Equation 2, so that they represent the total sediment load.

We calculated sediment load-weighted $[^{10}Be]_{m\text{-}DI}$ and $[^{9}Be]_{reac}$ values of 0.86×10^7 at g^{-1} and 2.19×10^{16}, respectively, for river km 0 (Table S2, Figures 2a and 2b). $[^{10}Be]_{m\text{-}DI}$ progressively increased downstream to a concentration of 2.99×10^7 at g^{-1} at km 1,221, representing a 231% overall increase (p value 3.0×10^{-4}, F test). Over the same distance, $[^{9}Be_{reac}]_{DI}$ increased more modestly, by 38%, from 2.19×10^{16} at g^{-1} to 3.03×10^{16} at g^{-1} at river km 1,221 (p value 0.051, F test) (Figure 2b). $(^{10}Be/^{9}Be)_{reac\text{-}DI}$ started at 3.81×10^{-10} at river km 0, and increased 145% over the 1,221 km transit distance (p value 2.2×10^{-3}, F test) (Figure 2c). $(^{10}Be/^{9}Be)_{reac\text{-}DI}$ decreased at river km 422, due to an increase in $[^{9}Be]_{reac}$ (Figure 2b). Downstream of this station, $(^{10}Be/^{9}Be)_{reac}$ values gradually increased to a final ratio of 9.37×10^{-10} at km 1,221. $[^{10}Be]_{norm\text{-}DI}$ increased from 0.90×10^7 at g^{-1} to 2.99×10^7 at g^{-1}, which represents a 232% increase over the entire transit distance (p value 2.0×10^{-4}, F test) (Figure 4a). While normalizing $[^{10}Be]_m$ to $[^{9}Be]$ increased the uncertainty on $[^{10}Be]_{norm}$ of individual samples, this treatment reduced the variability among samples within a given depth profile, thereby reducing the uncertainty of $[^{10}Be]_{norm\text{-}DI}$.

5.3. Estimated Local $F^{10}Be_m$

OSL ages constrain the minimum and maximum depositional ages for the floodplain sediment cores, with SP1 at 0.8–1.9 ka, SP2 at 13.3–20.2 ka, SP3 2.10–3.70 ka, and SP4 at 0.4–0.9 ka (Text S3, Table S3). SP1 and SP4 demonstrate exponential decline of $[^{10}Be]_m$ with increasing sediment depth (Figure 5, Table S4), which is typically observed in poorly-developed soils (Graly et al., 2010) and allows for derivation of the local $F^{10}Be_m$. SP2 and SP3 show more complicated concentration-depth distributions resulting from postdepositional erosion/burial, incomplete Be retention, or incomplete sampling of depth profiles (Text S3). SP1 has a $^{10}Be_m$ soil inventory of 5.68×10^9 at cm^{-2}, resulting in $F^{10}Be_m$ of 3.0×10^6 at cm^{-2} yr^{-1} averaged over the last 1.9 kyr (OSL age) (Equation 4). In agreement, SP4 has a $^{10}Be_m$ soil inventory of 2.56×10^9, which yields a $F^{10}Be_m$ of 2.85×10^6 at cm^{-2} yr^{-1} averaged over the last 0.9 kyr. In comparison, $F^{10}Be_m$ values from GCM-based datasets for the Rio Bermejo catchment range from 3.8×10^6 atoms cm^{-2} yr^{-1} in the headwaters to $2.4–2.7 \times 10^6$ atoms cm^{-2} yr^{-1}in the floodplain (Heikkila & von Blanckenburg, 2015), bracketing our sediment profile-derived $F^{10}Be_m$

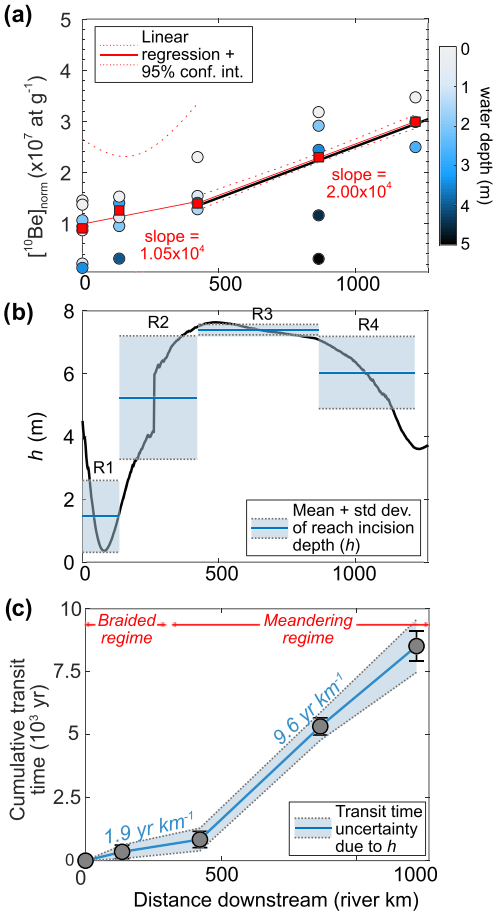

Figure 4. (a) $[^{10}Be]_{norm}$ and $[^{10}Be]_{norm\text{-}DI}$ (atoms g^{-1}), calculated using Equation 3, plotted against distance downstream. Circles represent individual samples, colored by depth below the water surface. Error bars on individual sample points represent the propagation of analytical uncertainty and weighted error. Red squares show the depth-integrated, normalized concentrations with error bars representing the root-mean-square errors of Equation 1, normalized by $[^{9}Be]_{reac}$. The red trend lines are linear regressions with 95% confidence interval fitted to the $[^{10}Be]_{norm\text{-}DI}$ data for the braided and meandering reaches, respectively. (b) Remobilization depth, *h*, measured along the channel (heavy black line) and mean remobilization depths for reaches 1–4 (R1–R4). (c) Cumulative transit time for each reach (heavy blue line) plotted against distance downstream, with minimum and maximum bounds associated with the standard deviation of *h* in each reach.

values. Because it averages over a longer time period than SP4, we use the $F^{10}Be_m$ value of 3.0×10^6 at cm^{-2} yr^{-1} from SP1 as input to the transit time model.

6. Estimating Sediment Transit Time With $^{10}Be_m$ Concentrations

To estimate the mean total sediment transit time, we employed Equation 5, translating the difference in $[^{10}Be]_{m\text{-}DI}$ between upstream and downstream stations into a measure of time. This requires constraining several parameters. For the initial and final $[^{10}Be]_m$, we use $[^{10}Be]_{norm\text{-}DI}$ values at the 0 and 1,221 km locations, respectively (Figure 4a, Table S2). $F^{10}Be_m$ for the Rio Bermejo floodplain is 3.0×10^6 at cm^{-2} yr^{-1}, as calculated from floodplain profile SP1. Rio Bermejo sediment is organic-poor, quartz-rich, and composed of ~15% clay, ~60% silt, and ~25% fine-medium sand, on average, suggesting a bulk density, ρ_s, of 1.5–2.0 g cm^{-3} (e.g., Snyder et al., 2004). We determined values for the remobilization depth, *h*, by DEM analysis of the incision depth of the channel into the floodplain, as described in the supporting information (Text S1). *h* ranged from 0.36 m in the foredeep to 8.2 m in the forebulge reaches of the river (Figure 4b), and we used the mean and standard deviation of this data set ($n = 694$), 6.1 ± 2.1 m, in our principal calculation.

The resulting mean transit time for the entire 1,221 km length of the Rio Bermejo is 8.4 ± 2.2 kyr (Figure 6, Table 1). According to this estimate, sediment is transported downstream at a virtual velocity (transit distance normalized by total transit time) of ~145 m yr^{-1}, which can also be interpreted as an average particle aging rate of 6.9 years km^{-1} (Table 1). Cumulative transit time increases with distance along the channel, but the downstream trend is different in the braided (foredeep) and meandering reaches (forebulge and backbulge), respectively (Figure 4c). Particles transiting the river system age at a rate of 1.9 yr km^{-1} through the superelevated, braided reach, and 9.6 yr km^{-1} through the meandering section (Figure 4c). The longer transit time through the meandering reach relative to the braided reach is consistent with superelevation of the foredeep channel keeping aged sediment out of the reach, while the high lateral migration rates in the incised meandering reach entrain stored floodplain sediment (Figure 7).

7. Discussion

7.1. Sensitivity of $^{10}Be_m$ as a Transit Time Tracer

The increase in $^{10}Be_m$ with distance downstream supports using $^{10}Be_m$ as a tracer to estimate mean sediment transit times. This technique provides a method to resolve lag times for signals propagating from upstream sediment sources to downstream sediment sinks (e.g., Romans et al., 2016), resolve time scales associated with biogeochemical cycling, and investigate the geomorphic and tectonic mechanisms that regulate transit time. However, before this method can be applied, several assumptions and underlying mechanisms of the $^{10}Be_m$ proxy need to be considered, as follows:

i. Our $^{10}Be_m$ transit time estimate of 8.4 ± 2.2 kyr represents the mean time particles spent in transit from river km 0 to river km 1,221. While this method cannot estimate the distribution of individual transit times for all particles traversing a system, multiple transit time distributions have been proposed, including exponential (Everitt, 1968; Nakamura & Kikuchi, 1996), power law (Lancaster et al., 2010; Pizzuto et al., 2017), and pareto (Ganti et al., 2011) distributions, while Bradley and Tucker (2013) suggest

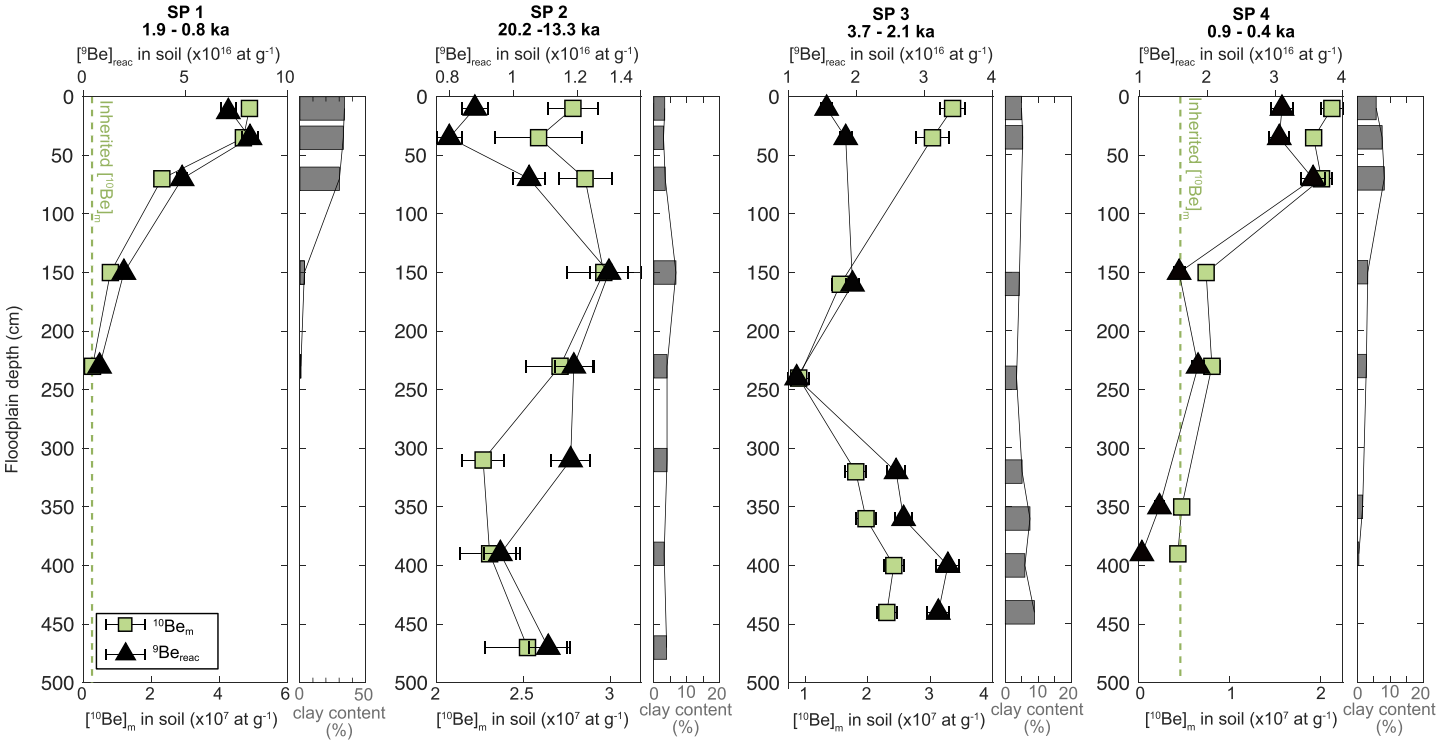

Figure 5. $[^{10}Be]_m$ (pale green squares), $[^{9}Be]_{reac}$ (black triangles), and clay content (<2 μm; gray bars) in floodplain sediment profiles SP1, 2, 3, and 4. Note differences in *x* axis scales. SP1 and SP4 demonstrate a typical exponential decrease in concentrations with depth, as shown in poorly developed soils by Graly et al. (2010).

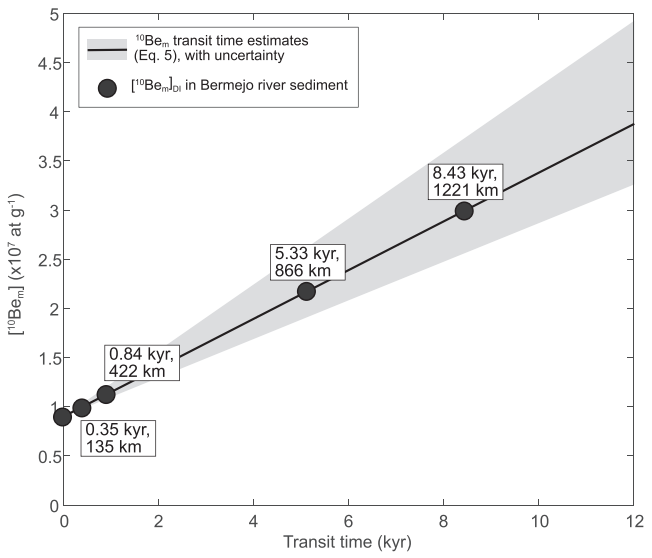

Figure 6. (a) A linear model of $[^{10}Be]_m$ in fluvial sediment through time, based on Equation 5. The solid black line shows the modeled evolution of $[^{10}Be]_{norm\text{-}DI}$ through time for the river mean remobilization depth of 6.03 ± 2.12 m (uncertainty shown by the gray-shaded region). Black circles show the measured $[^{10}Be]_{norm\text{-}DI}$ values at the mountain front and in the four depth profiles downstream. (b) Cumulative transit time, calculated as the sum of transit times for upstream reaches, plotted against distance downstream. Two linear fits describe the behavior of sediment transit in the predominantly braided regime (0–263 km) and meandering regime (264–1,267 km), respectively.

different distributions for different time scales. These distributions are often heavy-tailed, implying the $^{10}Be_m$-derived mean transit time of 8.4 kyr is likely biased toward a minor population of particles with long transit times, while most particles in the river have shorter transit times.

ii. The concentration of $^{10}Be_m$ in river sediment may depend on the abundance of secondary mineral coatings and particle surface area. In Rio Bermejo sediment, we observe a significant positive linear relationship between $[^{10}Be]_m$ and SSA (Figure 3), but not between $^{9}Be_{reac}$ and SSA. $^{9}Be_{reac}$ and SSA show greater variability within a depth profile than with distance downstream (Figure 2b), suggesting that changes in these $^{10}Be_m$-regulating parameters do not control the downstream increase in $[^{10}Be]_m$. Depth-integration characterizes the full suspended load, capturing the full range of concentration variability. ^{9}Be-normalization reduces $[^{10}Be]_m$ variability among samples within depth profiles, ultimately reducing the uncertainty of the depth-integrated $[^{10}Be]_{norm}$ values, and thus the estimated transit time (Figure 4a).

iii. On time scales up to 10^4 yr, all $^{10}Be_m$ delivered to the floodplain is retained in the sediment that is then eroded into the river. $^{10}Be_m$ retention on sedimentary particles can be influenced by pH, leaching intensity, and adsorption capacity in soil. Under acidic pH conditions or a positive water budget, $^{10}Be_m$ can desorb from particles or reactive phases can be mobilized to the dissolved phase (Dixon et al., 2018; von Blanckenburg et al., 2012). While floodplain soil pH was not measured for the Rio

Journal of Geophysical Research: Earth Surface

10.1029/2019JF005419

Table 1
Transit Time Estimates and Geomorphic Parameters for Reaches 1–4 and the Full River

River reach	Distance along channel	Reach length	Channel migration rate	h[a]	$[^{10}Be]_{norm\text{-}DI}$ initial	$[^{10}Be]_{norm\text{-}DI}$ final	$[^{10}Be]_{norm\text{-}DI}$ increase	Transit time through reach[b]	Cumulative transit Time[c]	Sediment aging rate	Virtual sediment velocity
	km	km	m yr^{-1}	m	$\times 10^7$ at g^{-1}	$\times 10^7$ at g^{-1}	$\times 10^7$ at g^{-1}	yr	yr	yr km^{-1}	m yr^{-1}
Reach 1	0–135	135	0	1.46 ± 1.15	0.90	1.25	0.35	350 ± 270	350 ± 270	2.6 ± 2.0	386 ± 168
Reach 2	135–422	287	28.1	5.26 ± 1.94	1.25	1.39	0.14	490 ± 180	840 ± 324	1.7 ± 0.6	586 ± 157
Reach 3	422–866	444	21.9	7.4 ± 0.17	1.39	2.29	0.90	4,490 ± 100	5,330 ± 340	10.1 ± 0.2	99.0 ± 2.25
Reach 4	866–1,221	355	6.26	6.83 ± 1.05	2.29	2.99	0.70	3,190 ± 490	8,520 ± 596	9.0 ± 1.4	111 ± 15.0
Full river length	0–1,221	1,221	23.23	6.03 ± 2.12	9.02	2.99	2.09	8,430 ± 2,200	8,520 ± 596	6.9 ± 1.8	145 ± 65.0

[a]Mean and standard deviation of incision depths along the channel. [b]Calculated using Equation 5 using parameters for each reach. [c]Calculated as the sum of upstream reach transit times, with uncertainty.

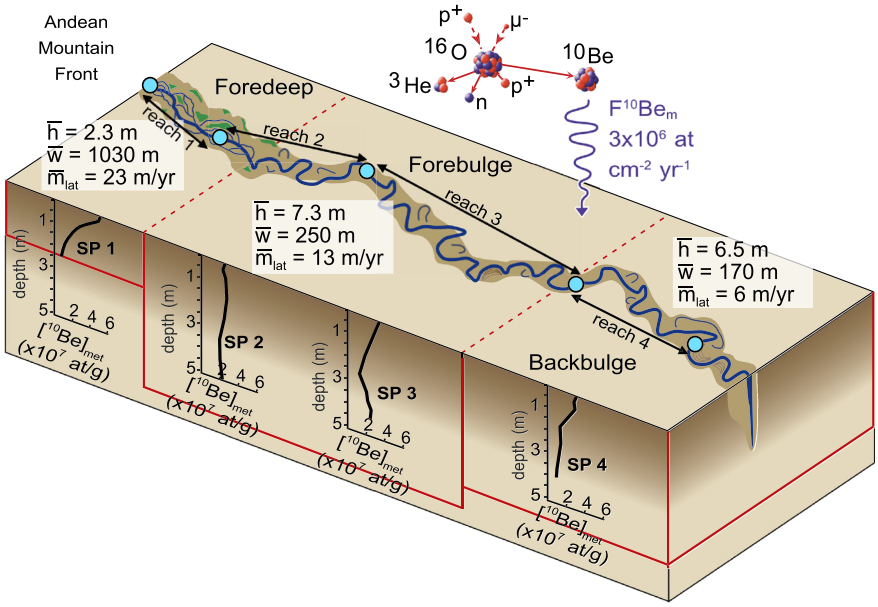

Figure 7. Schematic model of the Rio Bermejo system showing geomorphic constraints on the river system through the three morphotectonic domains of the Andean foreland basin. Shown in the white boxes are mean remobilization depth (h), channel width (w), and channel migration rate (m_{lat}) for the three domains (Text S1 in the supporting information). Blue circles indicate locations of river depth profiles, between which are reaches 1, 2, 3, and 4 where we evaluate differences in transit times and sediment storage dynamics. Red boxes delineate the remobilization depths for lateral channel-floodplain exchange in each depozone. $F^{10}Be_m$ is the flux of $^{10}Be_m$ from the atmosphere to the floodplain. ^{10}Be concentrations ($[^{10}Be]_m$) in floodplain soil profiles SP1 to SP4 are shown by the plots in the subsurface.

Bermejo, water measurements indicate consistent pH between 7.4 and 7.8 for Rio Bermejo river water, and higher pH values between 8 and 9 in local spring-fed streams (Table S1). Mean annual discharge is low at ~500 m^3 s^{-1}, and sediment export is high at ~100 Mt yr^{-1}, suggesting conditions for high Be retention (von Blanckenburg et al., 2012). Floodplain soils are poorly-developed due to the frequency of channel avulsions (Hartley et al., 2013), so $^{10}Be_m$ adsorption capacity should not be affected by strong soil development. In summary, while profiles SP1 and SP4 show consistent behavior, the difference exhibited in profiles SP2 and SP3 $[^{10}Be]_m$ (Figure 7) are likely due to the floodplain deposits having complex histories, including changes in inherited $[^{10}Be]_m$ due to translocation of 10Be to depths greater than those sampled or multiple depositional events. However, by sampling river suspended sediment depth profiles we capture the full range of variability among sediment transiting the Rio Bermejo.

iv. Constraining geomorphic variables used in Equation 5. The remobilization depth, h, has a significant impact on the resulting transit time because the total $^{10}Be_m$ inventory of the river suspended load is assumed to be distributed over one channel depth. We find that h ranges from ~2–7 m along the length of the river, and we use the standard deviation of the measured remobilization depths to constrain uncertainty on the total mean sediment transit time (Figure 4). h may be precisely constrained for any river system, using remote sensing methods or detailed field surveys (Text S1).

7.2. Comparison of $^{10}Be_m$ Transit Times to Sediment Budget-Based Predictions

To support that our $^{10}Be_m$-derived transit time estimate is reasonable, here we compare our results to channel belt and fluvial fan storage times estimated with simple sediment budgeting methods (e.g., Jerolmack & Mohrig, 2007; Pizzuto et al., 2014; Torres et al., 2017), the full details of which are described in the supporting information (Text S4, Tables S5 and S6). We assume a conceptual model where a lowland alluvial river migrates laterally across a narrow active channel belt within a wider fluvial fan. Between periodic river avulsions, sediment is reworked exclusively within the active channel belt as it is deposited and reentrained several times during downstream transit. Periodic avulsions allow the channel belt to occupy new areas of the

fan, and this process is repeated until the entire fan surface is reworked. This conceptual model allows for two separate transit time estimates, providing minimum and maximum bounds on the total mean sediment transit time. To constrain the minimum transit time, we estimate a characteristic length scale for particle transport between periods of deposition, x_{trans}, of ~280 km (Equation S3) (cf. Torres et al., 2017). Over the 1,221 km Rio Bermejo transit distance, sediment thus averages $n_{trans} \approx 4.4$ cycles of erosion and deposition (Equation S2). Stored sediment is remobilized at a time scale, $t_c \approx 0.14$ kyr, set by the average migration rate and channel width (Equation S4). Accordingly, we estimate a minimum transit time for sediment stored exclusively within the channel belt, $t_{belt} = n_{trans}\, t_c \approx 0.61$ kyr (Equation S5). Over longer time scales, we assume avulsions occur when the active channel belt aggrades one channel depth, yielding a characteristic avulsion recurrence interval, $t_a \approx 0.41$ kyr (Equation S7). For the Rio Bermejo, $t_a < t_{belt}$, suggesting the channel must reoccupy previous positions before all sediment can be transported out of the system. Complete fan-resurfacing requires $N_a \approx 51$ avulsions, resulting in a maximum transit time estimate of $t_{fan} = N_a\, t_a \approx 21$ kyr. These estimates are consistent with the range of depositional ages for floodplain deposits SP1–SP4 (0.4–0.9 kyr to 13.3–20.2 kyr (OSL)).

These estimates of $t_{belt} \approx 0.61$ kyr and $t_{fan} \approx 21$ kyr bracket our $^{10}Be_m$-derived transit time of 8.4 ± 2.2 kyr, suggesting that sediment within the Rio Bermejo is a mixture of sediment stored for relatively short time scales within the modern channel belt and sediment stored over longer time scales outside of the channel belt. Indeed, in its present form, the Rio Bermejo frequently breaches the edge of its belt and erodes older deposits (Figure S5), thereby incorporating stored floodplain sediment, enriched in $^{10}Be_m$, into the active channel load and increasing the sediment transit time beyond our t_{belt} estimate. Comparing our sediment-budget and $^{10}Be_m$-derived transit time estimates suggests that the $^{10}Be_m$ method accurately captures this incorporation of aged sediment. Interpreting the mean $^{10}Be_m$ transit time of 8.4 ± 2.2 kyr as a result of binary mixing of young (mean t_{belt} ~ 0.61 kyr) and old (mean t_{fan} ~ 21 kyr) sediment reservoirs, we estimate that ~60 ± 10% of sediment in the active channel is derived from within the modern channel belt, and ~40 ± 10% from beyond the channel belt. These values seem reasonable given the frequency that the Rio Bermejo breaches the modern channel belt boundaries, as observed in satellite imagery (Figure S5), and are consistent with the tendency for migrating rivers to preferentially erode younger deposits (Bradley & Tucker, 2013). The agreement between $^{10}Be_m$-derived and sediment budget-based transit time estimates highlights the utility of the latter for simple constraint of bulk sediment transit times.

7.3. Tectonic and Morphodynamic Controls on Sediment Transit Times

During the wet season, water flowing through the Rio Bermejo mainstem channel at a velocity of 1 m s^{-1} takes about 14 days to travel from the Andean mountain front to the confluence with the Rio Paraguay. The sediment transit times estimated above therefore indicate that along the entire length of the mainstem Rio Bermejo, clastic particles spend 4–5 orders-of-magnitude more time in storage than in motion. Accordingly, $^{10}Be_m$-derived transit times intrinsically contain information about sediment storage dynamics, which can be extracted by estimating transit times at the reach scale. Below we assess these reach-specific transit time estimates with respect to the morphodynamics of each reach to describe extrinsic controls on fluvial sediment transit time.

The morphodynamics of the Rio Bermejo change as the river crosses three foreland depozones: (1) 0–175 km away from the mountain front (river km 0–263) is a braided, super-elevated channel traversing the foredeep basin, (2) 176–475 km from the mountain front (river km 264–867) is an incised, tightly meandering reach crossing the uplifting forebulge, with high channel migration rates (up to 50 m/yr), and (3) 476–695 km from the mountain front (river km 868–1,267) is an incised, sinuous reach with cohesive banks and low channel migration rates (0–10 m/yr) (Figure 7). Because the foredeep basin is overfilled, and the channel is braided with rapid lateral reworking and shallow remobilization depths, we hypothesize that sediment has a low probability of being stored on the floodplain for long time scales and subsequently remobilized. In the forebulge, high channel migration rates and deep incision depths suggest that river sediment experiences multiple deposition-erosion cycles, and thus sediment has a high probability of being deposited on the floodplain and stored for 10^2–10^4 yr. In the backbulge, channel migration rates are low due to more cohesive river banks, which should result in little channel-floodplain exchange and short transit times. In the following subsections, we evaluate the differences in $^{10}Be_m$-derived transit times calculated for four reaches in between our five sampling locations to constrain how sediment storage dynamics

differ across these three domains (Figure 7). To calculate reach-specific transit times, we employed Equation 5, using the $[^{10}Be]_{norm\text{-}DI}$ values at the upstream and downstream ends of the reach for $[^{10}Be_m]_{x=0}$ and $[^{10}Be_m]_{x>0}$, respectively.

7.3.1. Sediment Transit Through Reach 1 (Foredeep, Braided Channel)

Reach 1 (river km 0–135 km) is braided and spans the foredeep basin. We expect only a limited increase in $[^{10}Be]_{norm\text{-}DI}$, primarily driven by remobilization of sediment from levees fringing the active channel. These levees are likely not long-lived features, so sediment has a low probability of being stored there long-term. One exception sits between river km 35 and 70, where the right bank is elevated by a buried thrust fault and river sediments of a presumably older age are exposed. Indeed, we observe a 0.35×10^7 at g^{-1} increase in $[^{10}Be]_{norm\text{-}DI}$ and a mean remobilization depth of 1.46 ± 1.15 m (Figures 4a and 4b), which equates to a transit time of 350 ± 270 yr (Table 1). These results agree with our hypothesis, as sediment travels relatively rapidly through Reach 1, at a virtual velocity of 386 ± 168 m yr^{-1} and aging rate of 2.6 ± 2.0 yr km^{-1} (Table 1). However, this does not account for the sediment spilled into the surrounding, low-lying floodplain, from where the river cannot presently reentrain it. Fundamentally, the foredeep is a location of sediment storage on geological time scales, so the short sediment transit times measured by $^{10}Be_m$ reflect the dynamics of the active river channel belt, rather than overall fluvial fan transit and storage between avulsions.

7.3.2. Sediment Transit Through Reach 2 (Braided-Meandering Transition)

Through Reach 2 (river km 136–422), $[^{10}Be]_{norm\text{-}DI}$ increases by 0.14×10^7 at g^{-1} and the mean remobilization depth is 5.26 ± 1.94 m (Figures 4a and 4b), resulting in a transit time of 490 ± 180 yr (Table 1). Here, the channel transitions from braided to meandering as it crosses from the foredeep into the forebulge depozone (McGlue et al., 2016) (Figure 7). Sediment transport capacity increases through this reach due to narrowing and deepening of the channel, at an approximately constant channel slope, and reduced channel belt width drives the reduction of accommodation space within the active channel belt. These factors all contribute to a relatively high virtual sediment velocity of 590 ± 160 m yr^{-1} and aging rate of only 1.7 ± 0.6 yr km^{-1}. Mobilization of stored sediment exposed in cut banks with known OSL ages of up to 13.3–20.2 kyr (Table S3) drives the increase of $[^{10}Be]_{norm}$. Although such banks exist along ~65% of Reach 2, the relatively high virtual sediment velocity suggests that reentrainment of aged river sediment by lateral channel migration and/or downcutting is limited, consistent with the tendency of migrating rivers to erode most rapidly through the youngest deposits (Bradley & Tucker, 2013).

7.3.3. Sediment Transit Through Reach 3 (Forebulge, Meandering Channel)

The greatest increase in $[^{10}Be]_{norm}$ is 0.90×10^7 at g^{-1} in reach 3 (river km 422–866, forebulge), resulting in a transit time of 4.49 ± 0.1 kyr, using a remobilization depth of 7.40 ± 0.17 m (Figures 4a and 4b, Table 1). This is the most deeply incised segment of the river, with a narrower active channel belt than in Reach 2. Channel migration rates are high, 10–50 m yr^{-1} (Text S1), indicating sediment is frequently exchanged between the channel and floodplain. These factors would act to reduce the sediment transit time. However, the significant increase of $[^{10}Be]_{norm\text{-}DI}$ compared to Reach 2, and the associated high aging rate of 10.1 ± 0.2 yr km^{-1} suggest that a large component of the river sediment load is mobilized from stored deposits outside the margins of the active channel belt. Consequently, erosion-deposition cycles cause "younger" particles to be deposited on point bars and "older" particles to be reentrained. According to our data, the forebulge is an erosional zone where particles are removed from long-term storage in the fluvial fan via lateral migration.

7.3.4. Sediment Transit Through Reach 4 (Backbulge, Meandering Channel)

Reach 4 (river km 867–1,221) has a $[^{10}Be]_{norm\text{-}DI}$ increase of 0.70×10^7 at g^{-1} and a mean remobilization depth of 6.83 m (Figures 4a and 4b), resulting in an estimated transit time of 3.19 ± 0.49 kyr (Table 1). This suggests a relatively high aging rate of 9.0 ± 1.4 yr km^{-1}, despite low channel migration rates. The long transit time through this reach suggests that, like in Reach 3, the active channel remobilizes old fan deposits that have aged significantly in now abandoned channel belts, as demonstrated by the floodplain sediment OSL ages (Table S3). The rate of channel migration in Reach 4 is low compared to upstream reaches, ~6.5 m yr^{-1} (Table 1), suggesting limited reentrainment of stored particles, so apparent transit through this reach should be short in comparison to Reach 3. However, the strong downstream increase in $[^{10}Be]_m$ indicates that the channel must be mobilizing stored sediment with a significantly older mean age in the few places with active lateral migration.

7.4. The Utility of $^{10}Be_m$ to Study Fluvial Processes

Our analysis of the geomorphic control on $^{10}Be_m$-derived transit times across the Andean foreland basin reveals the ability of $^{10}Be_m$ concentrations to resolve the mean fluvial sediment transit time over 10^3–10^5 yr time scales. While there are limitations to the $^{10}Be_m$ transit time method, it overcomes many challenges faced by other approaches. Estimating fluvial sediment transit times with a sediment budget-based approach provides only coarse bounds on transit time, as input parameters (e.g., Q_s, m_{lat}, w_{chan}) are naturally variable and cannot be confidently constrained over 10^2–10^5 yr. While the $^{10}Be_m$ method cannot resolve the full transit time distribution, the catchment-integrated sampling approach is a more efficient way to ascertain the mean transit time than comprehensive dating of floodplain deposits. Accurate assessment of biogeochemical cycling and sedimentary signal propagation require chronometers, like $^{10}Be_m$, which can estimate sediment transit duration over the same time scales that chemical reactions take place and signals are dampened. While we demonstrated the efficacy of this method in a simple river system, the next challenge is to apply the method to dendritic channel networks. In more complex settings, upstream and downstream $[^{10}Be]_m$ data may be used to simply estimate basin-averaged bulk sediment transit times, or to determine transit times within individual reaches between tributary junctions. To try to resolve the full transit time distribution, it may be possible to apply the method to grain size fractions and calculate a $^{10}Be_m$ transit time for each individual size class. For smaller river systems, our approach may also be applied using cosmogenic radionuclides having shorter half-lives, such as ^{7}Be and ^{137}Cs, which are also incorporated into the reactive phase. Additionally, we see the potential for using $^{10}Be_m$ transit time data to test existing transit time models and identify zones of storage that should be modeled (e.g., Czuba et al., 2015; Murphy et al., 2019).

8. Conclusions

We demonstrated the potential of meteoric cosmogenic ^{10}Be ($^{10}Be_m$) as a proxy to estimate fluvial sediment transit time in a large river system and combined that data with measurements of channel geometry and lateral migration rates to evaluate the controls on transit time. We measured $[^{10}Be]_m$ in suspended sediment river depth profiles collected from the Rio Bermejo, a large lowland alluvial river that traverses ~1,200 km from the Eastern Andean mountain front to its confluence with the Rio Paraguay with no tributaries. We observed a strong increase in depth-integrated $[^{10}Be]_m$ with increasing transit distance, and used this increase to estimate a mean sediment transit time of 8.4 $\pm$ 2.2 kyr. This estimated mean transit time is within bounds of sediment budget-based estimates that use geomorphic input parameters such as sediment flux, channel migration rate, and channel avulsion time scale. We compared $^{10}Be_m$-derived transit times for superelevated and braided vs. incised and meandering reaches, and for reaches with high versus low lateral migration rates, revealing that braided channels exhibit less floodplain storage than laterally migrating channels.

Using $^{10}Be_m$ as a transit time tracer has advantages over other geochemical transit time methods. The method is neither grain size-, nor mineralogy-specific (Willenbring & von Blanckenburg, 2010). The half-life of ^{10}Be is sufficiently long relative to fluvial sediment transit, such that decay of $^{10}Be_m$ in river sediment is negligible. Measuring concentrations in depth-integrated suspended sediment samples allows us to characterize the full sediment load, from fine wash load to coarse sandy bed sediment, as previously shown by Wittmann et al. (2015). Challenges of using $^{10}Be_m$ as a transit time tracer include constraining the depositional flux of $^{10}Be_m$ ($F^{10}Be_m$) in the local floodplain and the potential for pedogenic ^{10}Be loss in high precipitation-low pH settings, which can be resolved by collecting additional geochemical data for floodplain deposits.

In conclusion, this study provides the first systematic application of $^{10}Be_m$ as a sediment transit time tracer in a field setting. We built a framework for new applications of $^{10}Be_m$ to study fluvial sediment routing and to constrain time-dependent geochemical processes transpiring in lowland river floodplains, such as weathering and organic carbon oxidation. Furthermore, we show that combining geochemical data and geomorphic measurements can provide new insight on river responses to climatic and tectonic processes.

Acknowledgments

This study was funded by the Deutsche Forschungsgemeinschaft (DFG) Grant STR 373/34–1 and the Brandenburg Ministry of Sciences, Research and Cultural Affairs (Germany) through the international research training group IGK2018 (StRATEGy), led by Manfred Strecker. We thank Steve Binnie and Stefanie Heinze at the University of Cologne Centre for Accelerator Mass Spectrometry for conducting ^{10}Be measurements, Daniel Montluçon at the ETH Zürich Biogeoscience laboratory for assistance with BET surface area analysis, and Christoff Andermann and Stefan Liening at GFZ Potsdam for assistance with hydrologic data analyses and grain size data measurement at the GFZ Sed Lab. Sample collection and channel depth measurements would not have been possible without field assistance from Roberto Lopez, Francisco Latosinski, and Hima Hassenruck-Gudipati. We thank Friedhelm von Blanckenburg and Jens Turowski for supportive discussions, and Jim Pizzuto, Joseph Graly, and one anonymous reviewer for comments that greatly improved the manuscript. Additional methods, figures, and data referred to in the main text are available in the supporting information file. Data can be accessed at this site (https://doi.pangaea.de/10.1594/PANGAEA.913993).

References

Armitage, J. J., Duller, R. A., Whittaker, A. C., & Allen, P. A. (2011). Transformation of tectonic and climatic signals from source to sedimentary archive. *Nature Geoscience*, *4*(4), 231–235. https://doi.org/10.1038/ngeo1087

Belmont, P., Willenbring, J. K., Schottler, S. P., Marquard, J., Kumarasamy, K., & Hemmis, J. M. (2014). Toward generalizable sediment fingerprinting with tracers that are conservative and nonconservative over sediment routing timescales. *Journal of Soils and Sediments*, *14*(8), 1479–1492. https://doi.org/10.1007/s11368-014-0913-5

Bouchez, J., Lupker, M., Gaillardet, J., France-Lanord, C., & Maurice, L. (2011). How important is it to integrate riverine suspended sediment chemical composition with depth? Clues from Amazon River depth-profiles. *Geochimica et Cosmochimica Acta*, *75*(22), 6955–6970. https://doi.org/10.1016/j.gca.2011.08.038

Bradley, D. N., & Tucker, G. E. (2013). The storage time, age, and erosion hazard of laterally accreted sediment on the floodplain of a simulated meandering river. *Journal of Geophysical Research: Earth Surface*, *118*, 1308–1319. https://doi.org/10.1002/jgrf.20083

Brunauer, S., Emmett, P. H., & Teller, E. (1938). Adsorption of Gases in Multimolecular Layers. *Journal of the American Chemical Society*, *60*(2), 309–319. https://doi.org/10.1021/ja01269a023

Chmeleff, J., von Blanckenburg, F., Kossert, K., & Jakob, D. (2010). Determination of the ^{10}Be half-life by multicollector ICP-MS and liquid scintillation counting. *Nuclear Instruments and Methods in Physics Research, Section B: Beam Interactions with Materials and Atoms*, *268*(2), 192–199. https://doi.org/10.1016/j.nimb.2009.09.012

Cohen, A., McGlue, M. M., Ellis, G. S., Zani, H., Swarzenski, P. W., Assine, M. L., & Silva, A. (2015). Lake formation, characteristics, and evolution in retroarc deposystems. *A synthesis of the modern Andean orogen and its associated basins*, *1212*(16), 309–335. https://doi.org/10.1130/2015.1212

Czuba, J. A., Foufoula-Georgiou, E., Clark, M. P., Nijssen, B., Lundquist, J. D., Kavetski, D., et al. (2015). Water resources research. *Water Resources Research*, *51*, 2498–2514. https://doi.org/10.1002/2015WR017200.A

Dade, W. B., & Friend, P. F. (1998). Grain-size, sediment-transport regime, and channel slope in alluvial rivers. *Journal of Geology*, *106*(6), 661–676. https://doi.org/10.1086/516052

DePaolo, D. J., Maher, K., Christensen, J. N., & McManus, J. (2006). Sediment transport time measured with U-series isotopes: Results from ODP North Atlantic drift site 984. *Earth and Planetary Science Letters*, *248*(1-2), 394–410. https://doi.org/10.1016/j.epsl.2006.06.004

Dewald, A., Heinze, S., Jolie, J., Zilges, A., Dunai, T., Rethemeyer, J., et al. (2013). CologneAMS, a dedicated center for accelerator mass spectrometry in Germany. *In Nuclear Instruments and Methods in Physics Research, Section B: Beam Interactions with Materials and Atoms*, *294*, 18–23. https://doi.org/10.1016/j.nimb.2012.04.030

Dixon, J. L., Chadwick, O. A., & Pavich, M. J. (2018). Climatically controlled delivery and retention of meteoric 10Be in soils. *Geology*, *46*(10), 899–902. https://doi.org/10.1130/G45176.1

Dosseto, A., Bourdon, B., & Turner, S. P. (2008). Uranium-series isotopes in river materials: Insights into the timescales of erosion and sediment transport. *Earth and Planetary Science Letters*, *265*(1-2), 1–17. https://doi.org/10.1016/j.epsl.2007.10.023

Egli, M., Brandová, D., Böhlert, R., Favilli, F., & Kubik, P. W. (2010). 10Be inventories in Alpine soils and their potential for dating land surfaces. *Geomorphology*, *119*(1-2), 62–73. https://doi.org/10.1016/j.geomorph.2010.02.019

Everitt, B. L. (1968). Use of the cottonwood in an investigation of the recent history of a flood plain. *American Journal of Science*, *266*(6), 417–439. https://doi.org/10.2475/ajs.266.6.417

Frings, R. M. (2008). Downstream fining in large sand-bed rivers. *Earth-Science Reviews*, *87*(1–2), 39–60. https://doi.org/10.1016/j.earscirev.2007.10.001

Ganti, V., Straub, K. M., Foufoula-Georgiou, E., & Paola, C. (2011). Space-time dynamics of depositional systems: Experimental evidence and theoretical modeling of heavy-tailed statistics. *Journal of Geophysical Research: Earth Surface*, *116*, F02011. https://doi.org/10.1029/2010JF001893

Graly, J. A., Bierman, P. R., Reusser, L. J., & Pavich, M. J. (2010). Meteoric ^{10}Be in soil profiles - a global meta-analysis. *Geochimica et Cosmochimica Acta*, *74*(23), 6814–6829. https://doi.org/10.1016/j.gca.2010.08.036

Graly, J. A., Reusser, L. J., & Bierman, P. R. (2011). Short and long-term delivery rates of meteoric ^{10}Be to terrestrial soils. *Earth and Planetary Science Letters*, *302*(3-4), 329–336. https://doi.org/10.1016/j.epsl.2010.12.020

Granet, M., Chabaux, F., Stille, P., Dosseto, A., France-Lanord, C., & Blaes, E. (2010). U-series disequilibria in suspended river sediments and implication for sediment transfer time in alluvial plains: The case of the Himalayan rivers. *Geochimica et Cosmochimica Acta*, *74*(10), 2851–2865. https://doi.org/10.1016/j.gca.2010.02.016

Gray, H. J., Tucker, G. E., & Mahan, S. A. (2018). Application of a luminescence-based sediment transport model. *Geophysical Research Letters*, *45*, 6071–6080. https://doi.org/10.1029/2018GL078210

Gray, H. J., Tucker, G. E., Mahan, S. A., McGuire, C., & Rhodes, E. J. (2017). On extracting sediment transport information from measurements of luminescence in river sediment. *Journal of Geophysical Research: Earth Surface*, *122*, 654–677. https://doi.org/10.1002/2016JF003858

Handley, H. K., Turner, S., Afonso, J. C., Dosseto, A., & Cohen, T. (2013). Sediment residence times constrained by uranium-series isotopes: A critical appraisal of the comminution approach. *Geochimica et Cosmochimica Acta*, *103*, 245–262. https://doi.org/10.1016/j.gca.2012.10.047

Hartley, A. J., Weissmann, G. S., Bhattacharyya, P., Nichols, G. J., Scuderi, L. A., Davidson, S. K., et al. (2013). Soil development on modern distributive fluvial systems: Preliminary observations with implications for interpretation of Paleosols in the rock record. *In New Frontiers in Paleopedology and Terrestrial Paleoclimatology: Paleosols and Soil Surface Analog Systems*, 149–158. https://doi.org/10.2110/sepmsp.104.10

Heikkila, U., & von Blanckenburg, F. (2015). *The global distribution of Holocene meteoric ^{10}Be fluxes from atmospheric models. Distribution maps for terrestrial Earths surface applications*. GFZ Data Services. https://doi.org/10.5880/GFZ.3.4.2015.001

Horton, B., & DeCelles, P. (1997). The modern foreland basin system adjacent to the Central Andes. *Geology*, *25*(10), 895. https://doi.org/10.1130/0091-7613(1997)025<0895:TMFBSA>2.3.CO;2

Horton, B. K., & Decelles, P. G. (2001). Modern and ancient fluvial megafans in the foreland basin system of the Central Andes, southern Bolivia: Implications for drainage network evolution if foldthrust belts. *Basin Research*, *13*(1), 43–63. https://doi.org/10.1046/j.1365-2117.2001.00137.x

Iriondo, M. H. (2007). In M. H. Iriondo, J. C. Paggi, & M. J. Parma Geomorphology. (Eds.), *The Middle Paraná River: Limnology of a subtropical wetland* (pp. 33–51). Berlin Heidelberg: Springer. https://www.springer.com/gp/book/9783540706236

Jelinski, N. A., Campforts, B., Willenbring, J. K., Schumacher, T. E., Li, S., Lobb, D. A., et al. (2019). Meteoric Beryllium-10 as a tracer of erosion due to Postsettlement land use in West-Central Minnesota, USA. *Journal of Geophysical Research: Earth Surface*, *124*, 874–901. https://doi.org/10.1029/2018JF004720

Jerolmack, D. J., & Mohrig, D. (2007). Conditions for branching in depositional rives. *Geology*, *35*(5), 463–466. https://doi.org/10.1130/G23308A.1

Jerolmack, D. J., & Paola, C. (2010). Shredding of environmental signals by sediment transport. *Geophysical Research Letters*, *37*, L19401. https://doi.org/10.1029/2010GL044638

Korschinek, G., Bergmaier, A., Faestermann, T., Gerstmann, U. C., Knie, K., Rugel, G., et al. (2010). A new value for the half-life of ^{10}Be by heavy-ion elastic recoil detection and liquid scintillation counting. *Nuclear Instruments and Methods in Physics Research, Section B: Beam Interactions with Materials and Atoms*, *268*(2), 187–191. https://doi.org/10.1016/j.nimb.2009.09.020

Lal, D., & Peters, B. (1967). Cosmic Ray Produced Radioactivity on the Earth. In K. Sitte (Ed.), *Encyclopedia of Physics*, *Cosmic Rays II* (Vol. 9, 46). Berlin, Heidelberg: Springer.

Lancaster, S. T., Underwood, E. F., & Frueh, W. T. (2010). Sediment reservoirs at mountain stream confluences: Dynamics and effects of tributaries dominated by debris-flow and fluvial processes. *Bulletin of the Geological Society of America*, *122*(11–12), 1775–1786. https://doi.org/10.1130/B30175.1

Lane, S. N., & Richards, K. S. (1997). Linking river channel form and process: Time, space and causality revisited. *Earth Surface Processes and Landforms*, *22*(3), 249–260. Retrieved from. https://onlinelibrary.wiley.com/doi/pdf/10.1002/%28SICI%291096-9837%28199703%2922%3A3%3C249%3A%3AAID-ESP752%3E3.0.CO%3B2-7

Lauer, J. W., & Parker, G. (2008). Modeling framework for sediment deposition, storage, and evacuation in the floodplain of a meandering river: Application to the Clark Fork River, Montana. *Water Resources Research*, *44*, W08404. https://doi.org/10.1029/2006WR005529

Martin, A. N., Dosseto, A., May, J. H., Jansen, J. D., Kinsley, L. P. J., & Chivas, A. R. (2019). Sediment residence times in catchments draining to the Gulf of Carpentaria, northern Australia, inferred by uranium comminution dating. *Geochimica et Cosmochimica Acta*, *244*, 264–291. https://doi.org/10.1016/j.gca.2018.09.031

McGlue, M. M., Smith, P. H., Zani, H., Silva, A., Carrapa, B., Cohen, A. S., & Pepper, M. B. (2016). An integrated sedimentary systems analysis of the RíO Bermejo (Argentina): Megafan character in the overfilled southern Chaco Foreland Basin. *Journal of Sedimentary Research*, *86*(12), 1359–1377. https://doi.org/10.2110/jsr.2016.82

Monaghan, M. C., Krishnaswami, S., & Thomas, J. H. (1983). ^{10}Be concentrations and the long-term fate of particle-reactive nuclides in five soil profiles from California. *Earth and Planetary Science Letters*, *65*(1), 51–60. https://doi.org/10.1016/0012-821X(83)90189-9

Murphy, B. P., Czuba, J. A., & Belmont, P. (2019). Post-wildfire sediment cascades: A modeling framework linking debris flow generation and network-scale sediment routing. *Earth Surface Processes and Landforms*, *44*(11), 2126–2140. https://doi.org/10.1002/esp.4635

Nakamura, F., & Kikuchi, S. I. (1996). Some methodological developments in the analysis of sediment transport processes using age distribution of floodplain deposits. *Geomorphology*, *16*(2), 139–145. https://doi.org/10.1016/0169-555X(95)00139-V

Nishiizumi, K., Imamura, M., Caffee, M. W., Southon, J. R., Finkel, R. C., & McAninch, J. (2007). Absolute calibration of ^{10}Be AMS standards. *Nuclear Instruments and Methods in Physics Research, Section B: Beam Interactions with Materials and Atoms*, *258*(2), 403–413. https://doi.org/10.1016/j.nimb.2007.01.297

Phillips, J. D., Marden, M., & Gomez, B. (2007). Residence time of alluvium in an aggrading fluvial system. *Earth Surface Processes and Landforms*, *32*(2), 307–316. https://doi.org/10.1002/esp

Pizzuto, J., Keeler, J., Skalak, K., & Karwan, D. (2017). Storage filters upland suspended sediment signals delivered from watersheds. *Geology*, *45*(2), 151–154. https://doi.org/10.1130/G38170.1

Pizzuto, J., Schenk, E. R., Hupp, C. R., Gellis, A., Noe, G., Williamson, E., et al. (2014). Characteristic length scales and time-averaged transport velocities of suspended sediment in the mid-Atlantic region, USA. *Water Resources Research*, *50*, 790–805. https://doi.org/10.1002/2013WR014485

Rahaman, W., Wittmann, H., & von Blanckenburg, F. (2017). Denudation rates and the degree of chemical weathering in the Ganga River basin from ratios of meteoric cosmogenic 10 be to stable 9 be. *Earth and Planetary Science Letters*, *469*, 156–169. https://doi.org/10.1016/j.epsl.2017.04.001

Reusser, L., & Bierman, P. (2010). Using meteoric ^{10}Be to track fluvial sand through the Waipaoa River basin, New Zealand. *Geology*, *38*(1), 47–50. https://doi.org/10.1130/G30395.1

Reusser, L., Graly, J., Bierman, P., & Rood, D. (2010). Calibrating a long-term meteoric ^{10}Be accumulation rate in soil. *Geophysical Research Letters*, *37*, L19403. https://doi.org/10.1029/2010GL044751

Romans, B. W., Castelltort, S., Covault, J. A., Fildani, A., & Walsh, J. P. (2016). Environmental signal propagation in sedimentary systems across timescales. *Earth-Science Reviews*, *153*, 7–29. https://doi.org/10.1016/j.earscirev.2015.07.012

Rouse, H. (1937). Modern conceptions of the mechanics of turbulence. *Transactions of the American Society of Civil Engineers*, *102*, 463–543.

Sheets, B. A., Hickson, T. A., & Paola, C. (2002). Assembling the stratigraphic record: Depositional patterns and time-scales in an experimental alluvial basin. *Basin Research*, *14*(3), 287–301. https://doi.org/10.1046/j.1365-2117.2002.00185.x

Shen, C., Beer, J., Kubik, P. W., Suter, M., Borkovec, M., & Liu, T. S. (2004). Grain size distribution, 10Be content and magnetic susceptibility of micrometer–nanometer loess materials. *Nuclear Instruments and Methods in Physics Research Section B: Beam Interactions with Materials and Atoms*, *223-224*, 613–617. https://doi.org/10.1016/j.nimb.2004.04.113

Singleton, A. A., Schmidt, A. H., Bierman, P. R., Rood, D. H., Neilson, T. B., Greene, E. S., et al. (2017). Effects of grain size, mineralogy, and acid-extractable grain coatings on the distribution of the fallout radionuclides 7Be, 10Be, 137Cs, and 210Pb in river sediment. *Geochimica et Cosmochimica Acta*, *197*, 71–86. https://doi.org/10.1016/j.gca.2016.10.007

Snyder, N. P., Rubin, D. M., Alpers, C. N., Childs, J. R., Curtis, J. A., Flint, L. E., & Wright, S. A. (2004). Estimating accumulation rates and physical properties of sediment behind a dam: Englebright Lake, Yuba River, northern California. *Water Resources Research*, *40*. W11301. https://doi.org/10.1029/2004WR003279

Sternberg, H. (1875). Untersuchungen uber Langen- und Querprofil geschiebefuhrender Flusse. *Zeitschrift Fur Bauwesen*, *25*, 483–506.

Stout, J. C., Belmont, P., Schottler, S. P., & Willenbring, J. K. (2014). Identifying sediment sources and sinks in the Root River, Southeastern Minnesota. *Annals of the Association of American Geographers*, *104*(1), 20–39. https://doi.org/10.1080/00045608.2013.843434

Strong, N., Sheets, B., Hickson, T., & Paola, C. (2005). A mass-balance framework for quantifying downstream changes in fluvial architecture. *Spec. Publs Int. Ass. Sediment.*, *35*, 243–253. https://doi.org/10.1002/9781444304350.ch14

Torres, M. A., Limaye, A. B., Ganti, V., Lamb, M. P., West, A. J., & Fischer, W. W. (2017). Model predictions of long-lived storage of organic carbon in river deposits. *Earth Surface Dynamics*, *5*(4), 711–730. https://doi.org/10.5194/esurf-5-711-2017

von Blanckenburg, F., Bouchez, J., & Wittmann, H. (2012). Earth surface erosion and weathering from the ^{10}Be (meteoric)/^{9}Be ratio. *Earth and Planetary Science Letters*, *351-352*, 295–305. https://doi.org/10.1016/j.epsl.2012.07.022

Willenbring, J. K., & von Blanckenburg, F. (2010). Meteoric cosmogenic Beryllium-10 adsorbed to river sediment and soil: Applications for earth-surface dynamics. *Earth-Science Reviews*, *98*(1-2), 105–122. https://doi.org/10.1016/j.earscirev.2009.10.008

Wittmann, H., Oelze, M., Roig, H., & von Blanckenburg, F. (2018). Are seasonal variations in river-floodplain sediment exchange in the lower Amazon River basin resolvable through meteoric cosmogenic ^{10}Be to stable ^{9}Be ratios? *Geomorphology*, *322*(September), 148–158. https://doi.org/10.1016/j.geomorph.2018.08.045

Wittmann, H., Von Blanckenburg, F., Bouchez, J., Dannhaus, N., Naumann, R., Christl, M., & Gaillardet, J. (2012). The dependence of meteoric ^{10}Be concentrations on particle size in Amazon River bed sediment and the extraction of reactive ^{10}Be/^{9}Be ratios. *Chemical Geology*, *318-319*, 126–138. https://doi.org/10.1016/j.chemgeo.2012.04.031

Wittmann, H., Von Blanckenburg, F., Dannhaus, N., Bouchez, J., Gaillardet, J., Guyot, J. L., et al. (2015). A test of the cosmogenic ^{10}Be(meteoric)/^{9}Be proxy for simultaneously determining basin-wide erosion rates, denudation rates, and the degree of weathering in the Amazon basin. *Journal of Geophysical Research: Earth Surface*, *120*. 2498–2528. https://doi.org/10.1002/2015JF003581

References From the Supporting Information

Aitken, M. J. (1998). In *An introduction to optical dating: The dating of quaternary sediments by the use of photon-stimulated luminescence* (p. 267). Oxford: Oxford University Press.